aerospace

MDPI

Article

Finite Element Study on the Stiffness Variation Mechanisms of Radially Bolted Cylindrical–Cylindrical Shell Joints Under Transient Thermo-Mechanical Loading

Ning Guo *, Weizhen Yun, Shuo Zhang, Haoyu Du and Chao Xu

School of Astronautics, Northwestern Polytechnical University, Xi'an 710072, China; shuo_zhang@mail.nwpu.edu.cn (S.Z.)
* Correspondence: guoning@nwpu.edu.cn

Abstract

Radially bolted cylindrical–cylindrical shell joints are critical load-bearing components in aerospace vehicles. These joints experience complex thermo–mechanical environments during flight, where aerodynamic heating and mechanical loads jointly induce nonlinear deformation and stiffness variation through evolving interfacial contact states. To elucidate these mechanisms, this study develops a sequentially coupled thermo–mechanical finite-element framework to analyze the stiffness evolution of RBCCSJs under transient heating and combined mechanical loads (tension, compression, and bending). The results show that the global stiffness evolves through distinct contact-controlled stages (sticking → microslip → macroslip → mechanical bearing), producing pronounced nonlinear stiffness troughs spanning over two orders of magnitude. Under tension and bending, stiffness peaks during full sticking and decreases with slip, whereas under compression, it recovers earlier due to its end-face-bearing formation. Transient heating introduces two competing effects, thermal-expansion-induced frictional stiffening during short-term heating and temperature-dependent material softening during sustained exposure, leading to a 19.2–34% reduction in stiffness under steady thermal conditions. These findings clarify the dominant role of contact-state evolution and thermo–mechanical coupling in joint behavior and provide a quantitative analytical basis for enhancing the stiffness reliability and design optimization of aerospace bolted assemblies operating in transient thermal environments.

Keywords: radially bolted joints; cylindrical shells; thermo-mechanical coupling; stiffness variation; finite element analysis; aerospace structures

Check for updates

Academic Editor: Hyun-Ung Oh

Received: 1 November 2025
Revised: 19 December 2025
Accepted: 31 December 2025
Published: 31 December 2025

Copyright: © 2025 by the authors. Licensee MDPI, Basel, Switzerland. This article is an open access article distributed under the terms and conditions of the Creative Commons Attribution (CC BY) license.

1. Introduction

In aerospace structures, the main body of a vehicle is typically assembled from multiple slender cylindrical shells joined end-to-end [1–3]. Among various connection types, bolted joints are widely used at interstage interfaces due to their ease of assembly and disassembly, high reliability, and excellent sealing performance [4,5]. According to the orientation of the fastener axis relative to the vehicle's longitudinal axis, these joints can be classified into axial-type [6–11] and radial-type configurations [12–14]. Axial-type joints, such as bolted flange connections, feature fastener axes parallel to the body axis, while radially bolted cylindrical–cylindrical shell joints (RBCCSJs) adopt a lap-type geometry, where fasteners are oriented perpendicular to the vehicle axis.

Under actual flight conditions, aerospace structures are subjected to complex mechanical environments, including axial tensile/compressive forces induced by engine thrust and

bending moments generated during maneuvering. These external loads induce frictional slip, variable contact stiffness, and stick–slip transitions at the interfaces between shell segments, producing strongly nonlinear structural behavior that significantly affects the global stiffness characteristics of the assembly [15–18]. In addition, during high-speed or hypersonic flight, the structure experiences severe aerodynamic heating, and the interstage joints operate in elevated-temperature environments. When the external heat flux penetrates the thermal protection layer, the internal "cold-wall" structure is directly exposed to elevated temperatures, leading to time-dependent material degradation such as the reduction in the elastic modulus and variation in the thermal expansion coefficient [19,20]. Simultaneously, bolt preload relaxation, contact-surface expansion, and frictional state evolution further alter the mechanical response, reducing joint stiffness and, in extreme cases, leading to joint failure [21–24]. Consequently, for high-speed aerospace vehicles, the coupling of thermal and mechanical loads profoundly affects interstage connection performance, directly impacting structural safety and reliability.

Extensive research has been conducted on the stiffness characteristics of radially bolted joint structures at room temperature, revealing multiple factors influencing their mechanical performance. Li et al. [12,25] combined analytical and numerical approaches to investigate the load distribution of such joints under axial, bending, and shear loads, accounting for interfacial friction, and discussed the effects of bolt preload, friction coefficient, and countersink angle on their mechanical behavior. Zhang et al. [13] employed finite-element simulations to examine the stiffness behavior of radial joints with assembly clearance, demonstrating trilinear axial stiffness and linear lateral stiffness, and further proposed a simplified trilinear equivalent dynamic model based on these characteristics. Mohapatra et al. [14,26–28] developed a spring–mass-based modeling framework to construct a predictive stiffness model for radially bolted joints, achieving accurate stiffness estimations under varying preloads and external loads.

While the mechanical behavior of axial bolted flange joints at elevated temperatures has been extensively studied [29–32], research on radially bolted joint structures, the focus of this work, remains limited. Only a few studies have addressed the influence of thermal environments on the mechanical performance of bolted joints. Jaglinski et al. [33,34] observed significant preload loss in bolts subjected to prolonged high-temperature exposure due to creep and relaxation, and proposed a constitutive model for predicting preload decay. Kettler et al. [35] performed long-term temperature cycling tests combined with simulations, revealing the retention of residual stress through bolt creep. Coman et al. [36,37] integrated strain-gauge measurements with finite-element analysis to study the thermal effects on single-bolt lap joints, accurately predicting their nonlinear elastic behavior. Sasikumar et al. [38] numerically simulated the thermo–mechanical response of composite lap joints considering bolt preload, thermal steps, and static tension, and discussed the evolution of contact states during different loading stages.

Despite these advancements, the stiffness-degradation mechanisms of radially bolted socket–spigot joints under coupled thermo–mechanical loading remain insufficiently understood. In particular, the transient heat-transfer process, which typically occurs from the exterior aerodynamic surface to the interior structure in real aerospace interstage connections, has not yet been thoroughly modeled or analyzed. To address this gap, the present study develops a high-fidelity finite-element model of a radially bolted cylindrical–cylindrical shell joint incorporating external transient heat-transfer effects. The model is used to systematically investigate the evolution of tensile, compressive, and bending stiffness under coupled transient thermo–mechanical loading, to elucidate the underlying mechanisms of stiffness variation, and to provide a theoretical and engineering foundation

for the design and reliability optimization of aerospace interstage connections operating in complex thermal–mechanical environments.

2. Analytical Model and Finite Element Modeling

2.1. Analytical Model Description

This study investigates the evolution of connection stiffness in a typical radially bolted cylindrical-cylindrical shell joint (RBCCSJ) under combined transient thermal and mechanical loading, and elucidates the underlying mechanisms. Figure 1 illustrates a representative RBCCSJ commonly used in aerospace vehicles. The joint employs a socket–spigot configuration, in which the wall thicknesses of both the inner cylindrical shell (ICS) and outer cylindrical shell (OCS) are locally increased to enhance stiffness and improve load-transfer capability. Structural integrity is ensured by countersunk-head bolts engaging with anchor nuts to provide reliable preload and alignment.

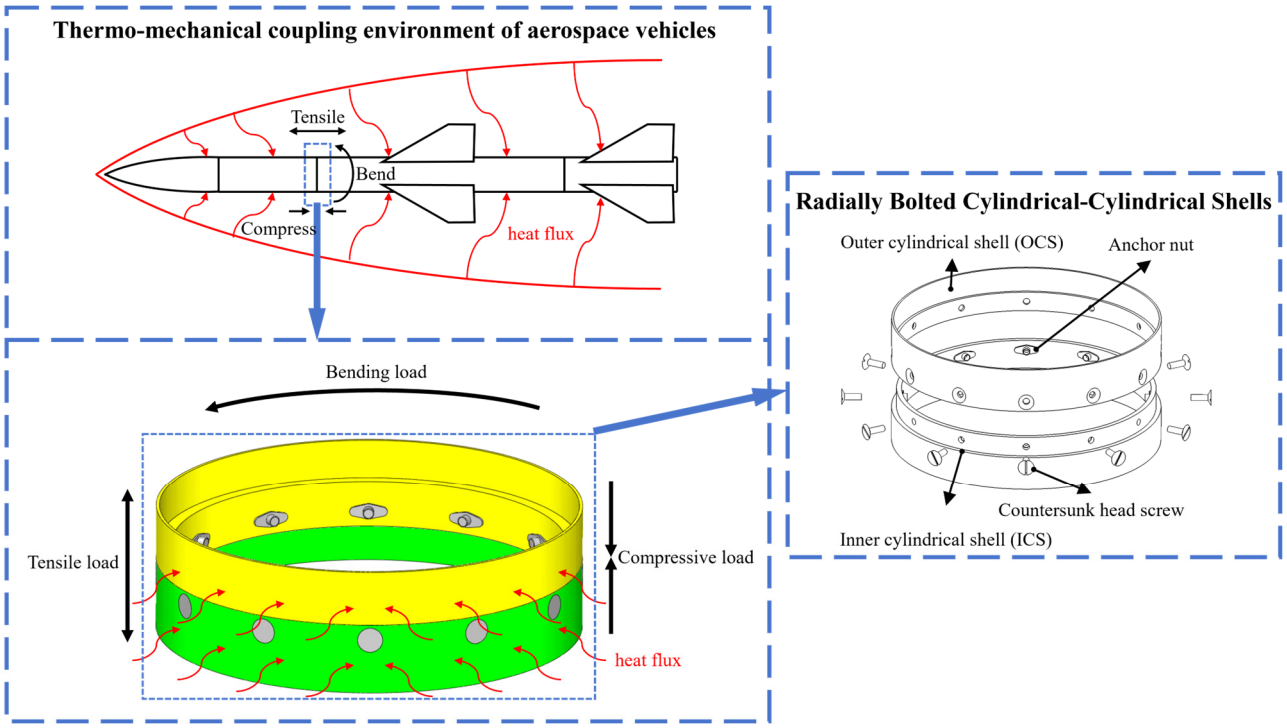


Figure 1. Representative RBCCSJ under thermo-mechanical coupling conditions.

Following standard engineering practice, the feedback effect of internal stress–strain on transient heat transfer is neglected, and a sequentially coupled thermo-mechanical analysis methodology is adopted. The analysis follows three steps: (i) a transient thermal analysis is first performed to obtain the temporal evolution of the temperature field; (ii) the temperature distribution within the specified heat transfer interval is mapped onto the static analysis model as a thermal load boundary condition; and (iii) under prescribed mechanical loading, the structural response and the evolution of connection stiffness in the RBCCSJ are evaluated. The details are shown in Figure 2.

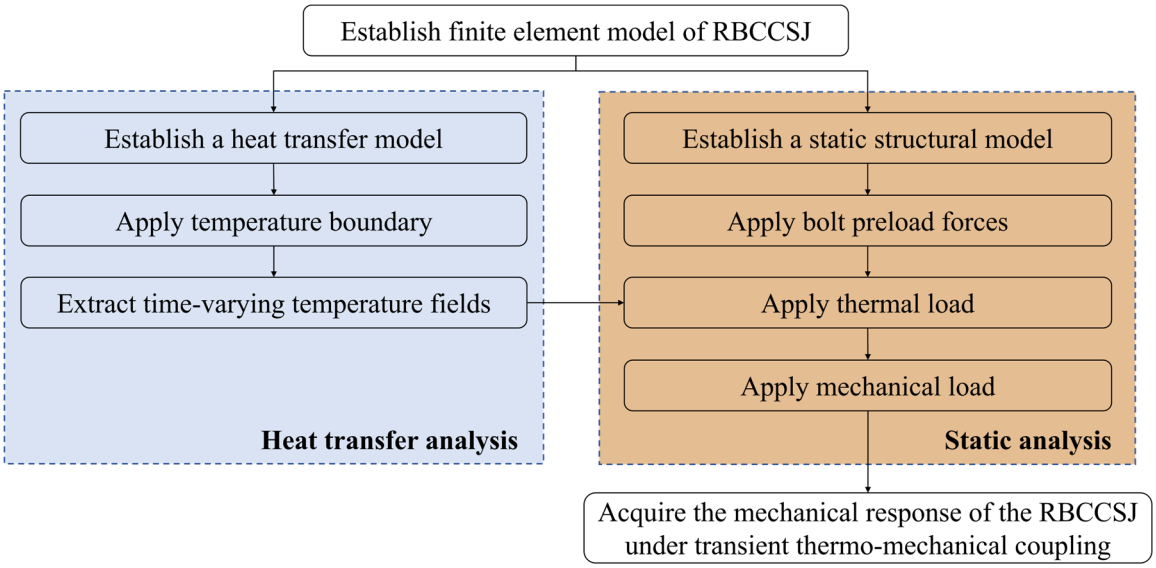


Figure 2. Sequential coupled thermo-mechanical analysis process for RBCCSJ.

The specific geometric and dimensions of the analytical model is illustrated in Figure 3. The cylindrical shells have an outer diameter of 300 mm and a nominal wall thickness of 2 mm, with the wall thickness in the connection region locally increased to 5 mm. Fastening is by standard M6 countersunk-head bolts (120° head angle) and anchor nuts. The hole diameter for the bolts is 6.6 mm. The bolts and nuts utilize AISI 304 stainless steel, whereas the cylindrical shell is constructed from 6061 aluminum alloy. The elastic–plastic properties of these materials are modeled using a bilinear constitutive relationship, as shown in Figure 4. The specific mechanical and thermal material properties are listed in Tables 1 and 2, respectively.

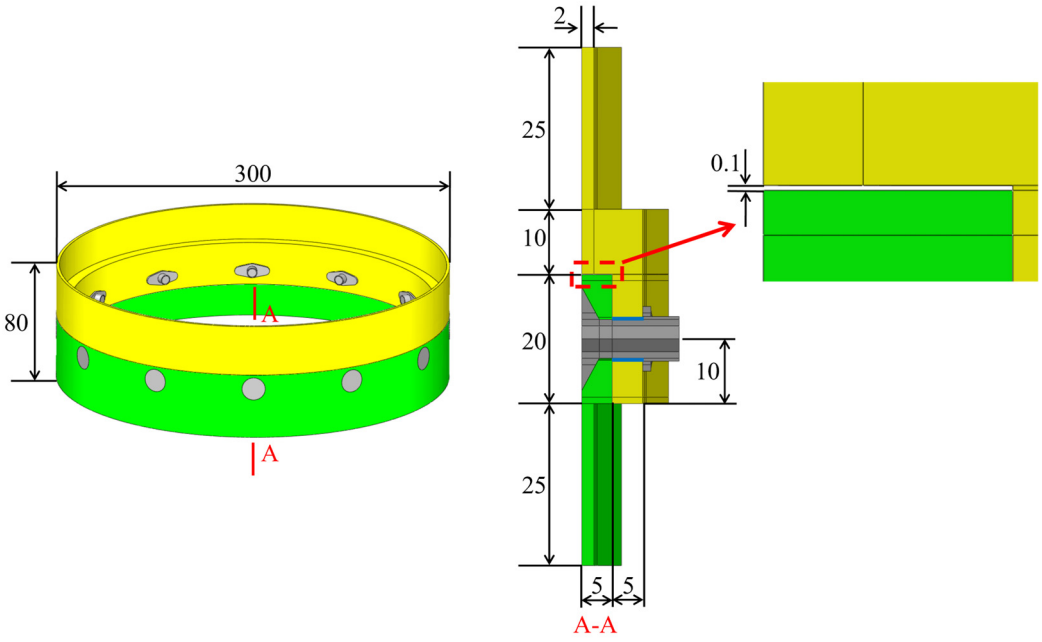


Figure 3. Geometric configuration and dimensions of the RBCCSJ.

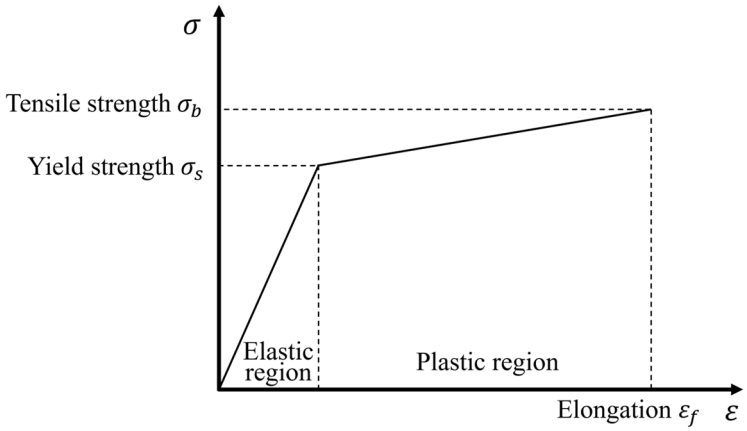


Figure 4. Bilinear constitutive model.

Table 1. Material mechanical property parameters.

Component	Material	Young's Modulus (MPa)	Poisson's Ratio	Density (t/mm^3)	Tensile Strength (MPa)	Yield Strength (MPa)	Elongation (%)
Cylindrical shell	AL 6061	68,900 (25 °C) 67,200 (50 °C) 64,800 (100 °C) 62,000 (150 °C) 58,600 (200 °C)	0.33	2.8×10^{-9}	310 (25 °C) 290 (100 °C) 230 (150 °C) 130 (200 °C)	276 (25 °C) 262 (100 °C) 214 (150 °C) 103 (200 °C)	17 (25 °C) 18 (100 °C) 20 (150 °C) 28 (200 °C)
Bolts and nuts	AISI 304	195,000 (25 °C) 192,000 (50 °C) 190,000 (100 °C) 186,000 (150 °C) 183,000 (200 °C)	0.29	7.85×10^{-9}	600 (25 °C) 565 (100 °C) 545 (150 °C) 530 (200 °C)	290 (25 °C) 255 (100 °C) 240 (150 °C) 225 (200 °C)	40 (25 °C) 42 (100 °C) 45 (150 °C) 50 (200 °C)

Table 2. Material thermal property parameters.

Component	Material	Specific Heat Capacity (mJ/(t·K))	Thermal Conductivity (mW/(mm·K))	Coefficient of Thermal Expansion (K^{-1})
Cylindrical shell	AL 6061	8.97×10^8 (25 °C) 9.02×10^8 (50 °C) 9.21×10^8 (100 °C) 9.46×10^8 (150 °C) 9.73×10^8 (200 °C)	167 (25 °C) 173 (50 °C) 177 (100 °C) 180 (150 °C) 186 (200 °C)	2.36×10^{-5} (25 °C) 2.41×10^{-5} (50 °C) 2.48×10^{-5} (100 °C) 2.54×10^{-5} (150 °C) 2.61×10^{-5} (200 °C)
Bolts and nuts	AISI 304	5.02×10^8 (25 °C) 5.05×10^8 (50 °C) 5.15×10^8 (100 °C) 5.25×10^8 (150 °C) 5.35×10^8 (200 °C)	15 (25 °C) 15.4 (50 °C) 16.1 (100 °C) 16.7 (150 °C) 17.3 (200 °C)	1.65×10^{-5} (25 °C) 1.68×10^{-5} (50 °C) 1.72×10^{-5} (100 °C) 1.76×10^{-5} (150 °C) 1.80×10^{-5} (200 °C)

2.2. Finite Element Modeling

A three-dimensional high-fidelity finite element model of the above analytical model is established in ABAQUS/CAE 2022 (Figure 5). To simplify the modeling process and improve computational efficiency, the detailed threads of screws and nuts are omitted. All structural components are discretized using hexahedral elements: DC3D8 (8-node thermal bricks) for the heat-transfer analysis and C3D8I (8-node bricks with incompatible modes) for the structural analysis (to prevent hourglass modes). The mesh is refined around the bolts and holes to capture stress concentrations and local deformation. When meshing the surfaces of a contact pair, matching the nodes one-to-one can significantly improve convergence. A mesh convergence study confirms the final mesh (498,590 elements, 613,896 nodes) is adequate (Table 3).

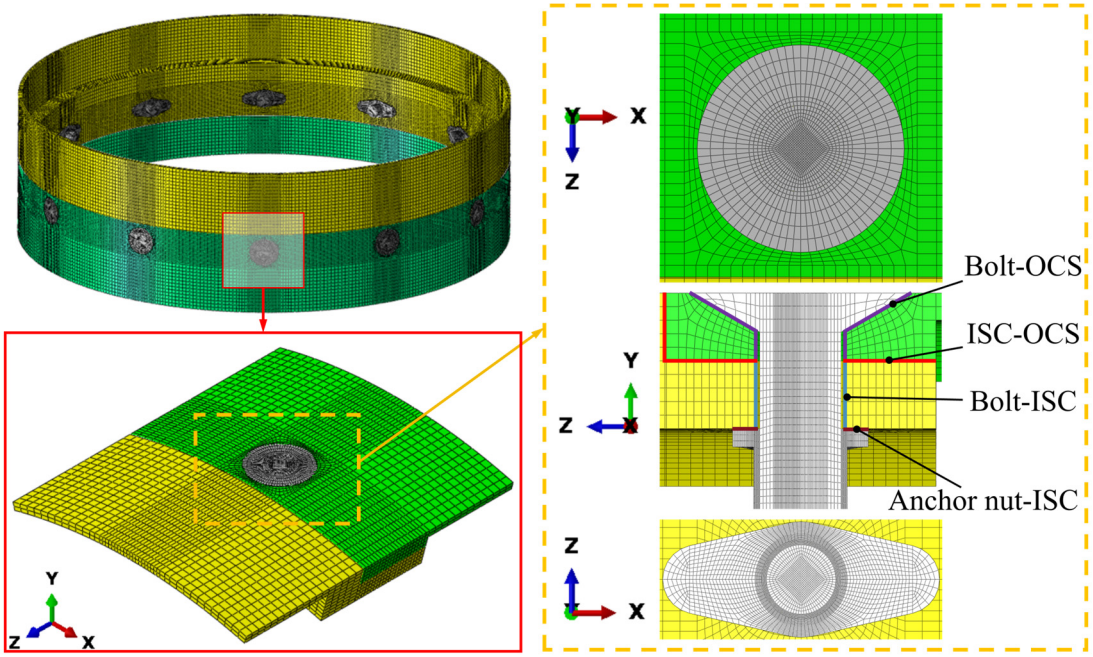


Figure 5. FE model of the RBCCSJ.

Table 3. Parameters of finite element model.

Component	Element Number	Node Number	Element Size (mm)	Jacobian Ratio
Outer cylindrical shell	78,912	106,488	0.13–2.24	0.36–1
Inner cylindrical shell	116,126	148,680	0.1–2.03	0.76–1
Bolt & Anchor nut	25,296	29,894	0.06–1.54	0.52–1
Total	498,590	613,896	0.06–2.24	0.36–1

According to the actual assembly and interaction conditions, contacts are defined between: (1) bolt-outer cylindrical shell (OCS), (2) bolt-inner cylindrical shell (ICS), (3) anchor nut-ICS, and (4) ISC-OCS, as shown in Figure 5. In the heat transfer analysis, the outward-to-inward heat conduction is modeled by applying a thermal contact conductance h_c (W/m^2 K) at interfaces. The value of h_c can be determined using an empirical relation that depends on the interfacial contact pressure [39]:

$$\begin{cases} h_c^{A-A} = 17574P^{0.94} \\ h_c^{A-S} = 5453P^{0.94} \end{cases} \quad (1)$$

where h_c^{A-A} and h_c^{A-S} represent the thermal contact conductance at the aluminum–aluminum interface, and at the aluminum–stainless steel interface, respectively, P represents the apparent contact pressure (MPa).

In the static structural analysis model, all contact interactions are defined as surface-to-surface, employing 'hard' normal behavior and 'Coulomb friction' tangential contact behavior (with a friction coefficient of μ = 0.2, adopted from empirical experience [2]). The contact constraints are enforced using a penalty function method.

In addition, the RBCCSJ has 12-fold cyclic symmetry, so under axial loading, a 1/12-segment finite element model with periodic boundary conditions is used (Figure 6). Under bending, this symmetry is broken, and the full finite element model is required.

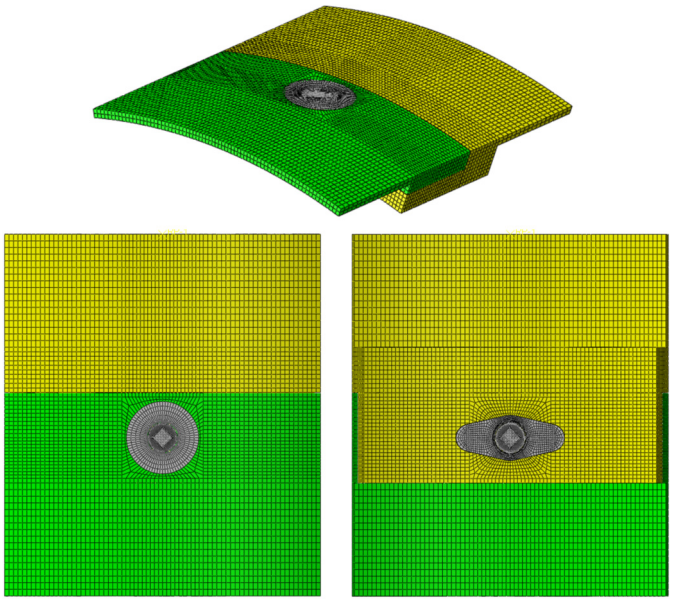


Figure 6. Finite element model of the 1/12 local RBCCSJ.

2.3. Thermo-Mechanical Coupling Analysis Procedure

Following the sequentially coupled thermo-mechanical analysis method described in Section 2.1, the process begins with a transient heat-transfer analysis. The aerodynamic heating transmitted through the vehicle's thermal protection layer to the structural surface is assumed to reach 200 °C (note: the cold-wall design temperature of aluminum alloy is generally 200 °C). The global initial structural temperature is set to 25 °C, and a boundary temperature of 200 °C is applied to the external surface. The resulting temperature field evolution with time is obtained from this step.

Subsequently, the static stiffness analysis is performed in three steps: Step 1—Bolt preload application: The tightening torque is set to 10 N·m, providing a safety margin relative to the known failure torque of 13 N·m for the M6 screws. According to internationally recognized design principles [40], this torque corresponds to an axial preload of 6500 N. A global initial temperature of 25 °C is also assigned in this step. Step 2—Thermal field application: The bolt load is then fixed at its current length. The transient temperature field corresponding to the selected heat-transfer time is introduced through the predefined field module, thereby applying the thermal load. Free-free boundary conditions are imposed to simulate the unconstrained thermal expansion state of the vehicle structure during flight. Step 3—Mechanical loading: Mechanical loads are applied at the coupling points on the structural loading surface. A continuous distribution coupling is used to avoid artificial thermal deformation constraints induced by coupling. In the bending simulation, the global model is employed, with fixed boundary conditions imposed on the structural support surface. In contrast, the 1/12 local model is used for the tension and the compression simulation, where axial displacement constraints are applied to the same surface and periodic boundary conditions are enforced on the cut section. The complete flowchart of the thermo-mechanical coupling analysis, along with all boundary condition settings, is presented in Figure 7. It should also be emphasized that nonlinear effects are fully considered throughout the entire analysis procedure.

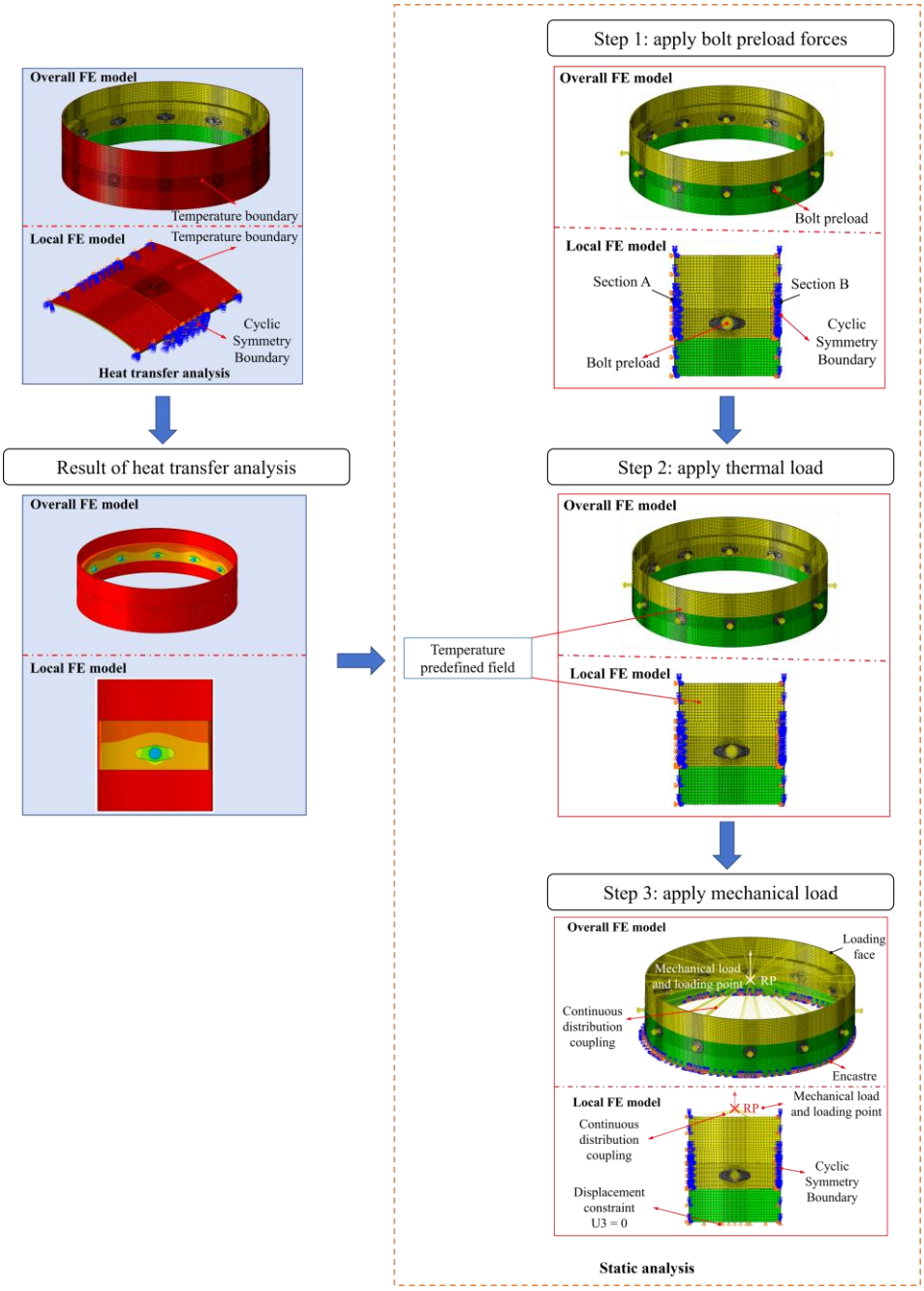


Figure 7. Flowchart of thermal–mechanical coupling analysis and boundary condition settings.

3. Analysis of Heat Transfer in the RBCCSJ Under Aerodynamic Heating

A transient heat-transfer analysis is performed with a uniform temperature boundary on the external surface. Figure 8 shows the structure's average temperature vs. time, with insets of the temperature field at representative times. The structure heats rapidly at first, then slowly approaches equilibrium. Three stages are identified:

Stage I—Rapid heat transfer stage (t < 10 s): The RBCCSJ undergo a sharp rise in average structural temperature, climbing from 25 °C to about 180 °C. This corresponds to an average heating rate of roughly 15.5 °C/s, nearly an order of magnitude faster than in subsequent stages. The inset temperature contours show that the OCS heats up much faster than the ICS and fasteners, producing a pronounced temperature difference (ΔT) between the components ($\Delta T \approx 104.2$ °C at 2 s). By 10 s, the shells nearly equilibrate (≈197.5 °C),

while the bolts remain ≈ 149.5 °C cooler. Surface heating and near-surface conduction dominate this stage.

Stage II—Transition stage (10 s ≤ t < 60 s): The average temperature increases gradually from ~180 °C to 200 °C, corresponding to a slower mean heating rate of approximately 0.4 °C/s. The slope of the curve shows clear exponential-type decay, consistent with Fourier heat conduction toward thermal equilibrium; the heat conduction along the bolt shank becomes an increasingly important pathway. The ΔT drops from 48 °C at 10 s to 0 °C at 60 s.

Stage III—Steady-state stage (t ≥ 60 s): The structure reaches thermal steady state at ~200 °C. The temperature is uniform across the OCS, inner shell, and bolts, with no significant ΔT.

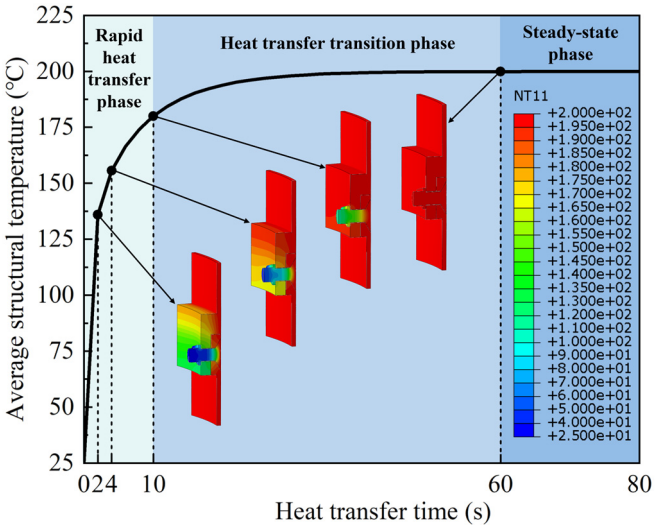


Figure 8. Evolution of the average temperature field of the RBCCSJ during heat transfer.

Based on these results, five representative thermal states are selected for subsequent structural stiffness analysis (Table 4). Each state provides a steady thermal field (the instantaneous temperature distribution from the thermal simulation) that is imposed as the thermal preload for mechanical analyses to determine tensile, compressive, and bending stiffness.

Table 4. Representative thermal conditions for stiffness analysis of the RBCCSJ.

Heat Transfer Time	Average Structural Temperature	Purpose of Analysis
0 s	25 °C	Baseline stiffness characteristics
2 s	136 °C	Initial rapid heat transfer
4 s	155.6 °C	Ongoing through-thickness conduction
10 s	180 °C	Near equilibrium of shells
60 s	200 °C	Fully stabilized temperature field

4. Mechanism Analysis of the Effects of Transient Thermo-Mechanical Coupling on Structural Connection Stiffness

4.1. Tensile Stiffness Mechanism

Based on the ultimate overload of 6 g (six times the gravitational acceleration) that actual aerospace vehicles may experience during flight, a linearly and uniformly increasing tensile load, up to 36 kN, is applied to the RBCCSJ. The tensile stiffness is defined as the ratio

of the load increment—taken as 1% of the maximum applied load—to the corresponding axial displacement increment:

$$\begin{cases} K_j^{\mathrm{T}} = \frac{F_j^{\mathrm{T}} - 0}{u_j^{\mathrm{T}} - 0}, j = 1 \\ K_j^{\mathrm{T}} = \frac{F_j^{\mathrm{T}} - F_{j-1}^{\mathrm{T}}}{u_j^{\mathrm{T}} - u_{j-1}^{\mathrm{T}}}, j = 2, 3, \ldots, n \end{cases} \quad (2)$$

where F_j^{T} and u_j^{T} denote the applied tensile load and the corresponding axial deformation of the coupling point at the j-th load increment, respectively; K_j^{T} is the tensile stiffness of the structure.

4.1.1. Under Ambient Temperature Conditions

Figure 9 illustrates the evolution of the structural tensile stiffness, component contact state, and axial deformation and stress distributions of the RBCCSJ under coupled axial tension and ambient temperature (25 °C) as the applied load increases. The tensile stiffness response shows a nonlinear evolution with increasing load, and can be divided into four characteristic stages (Figure 9a). Representative contact-state snapshots corresponding to the initial, intermediate, and final conditions of each stage are shown in Figure 9b. Here, 'O–B', 'I–O', 'I–A', 'T–B', and 'C–B' denote the contacts between the OCS and bolt, ICS and OCS, ICS and anchor nut, ICS through-hole wall and bolt, and ICS countersunk-hole wall and bolt, respectively. For convenience of representation, only half of the 'O-B' and 'I–O' contact surfaces are displayed, considering the structural symmetry. The axial deformation and stress distributions corresponding to the six identified stiffness transition points are presented in Figure 9c, where the OCS is half-cut for clarity. The detailed descriptions of each stage are as follows:

Stage I (Sticking stage): At low tensile loads (0–≈9.36 kN), the RBCCSJ exhibit a high and nearly linear stiffness response, maintaining an average tensile stiffness of approximately 5.13×10^2 kN/mm. During this stage, all primary interfaces ('O–B', 'I–O', and 'I–A') remain in a fully sticking condition, with negligible relative displacement among components. The axial deformation of the assembly is minimal, and the stress distribution is dominated by the bolt preload, indicating that the external tensile load is primarily resisted by interfacial friction and bolt pre-tension. Both the bolt shank and shell walls undergo uniform elastic deformation without any localized bending or stress concentration. As a result, the assembly behaves as a single, elastically coupled body, characterized by a linear load–stiffness relationship. This stage establishes the baseline stiffness of the structure, representing a fully coupled and friction-constrained state prior to the onset of interfacial microslip.

Stage II (Microslip stage): As the tensile load increases to approximately 18 kN, the global stiffness decreases sharply (from about 5.13×10^2 kN/mm to 1.75×10^2 kN/mm), signifying the onset of interfacial microslip. Localized slip initiates at the 'I–O' and 'C–B' interfaces, where the contact state gradually transitions from full sticking to partial slip, while the 'I–A' interface remains largely unaffected owing to the continuous compressive constraint imposed by the bolt preload. As slip zones expand radially, the effective load-transfer efficiency between the ICS and OCS decreases, leading to a pronounced stiffness reduction. The stress field exhibits noticeable local variations, with stress concentration observed near the ICS–OCS contact regions, accompanied by evident axial deformation. These localized kinematic inconsistencies indicate a loss of synchronous deformation between the ICS and OCS, resulting in partial load redistribution along the contact interfaces.

This stage represents a transition from a fully coupled to a partially decoupled contact state, in which frictional slip becomes the dominant mechanism governing energy

dissipation and stiffness degradation. As the microslip regions coalesce into larger slip zones, the degradation rate accelerates, reducing the effective stiffness and initiating the first nonlinear softening phase of the system. Despite the observed decline, the overall contact integrity of the joint remains intact, and the structure retains a residual load-bearing capacity supported by the still-sticking inner interfaces and the sustained bolt preload.

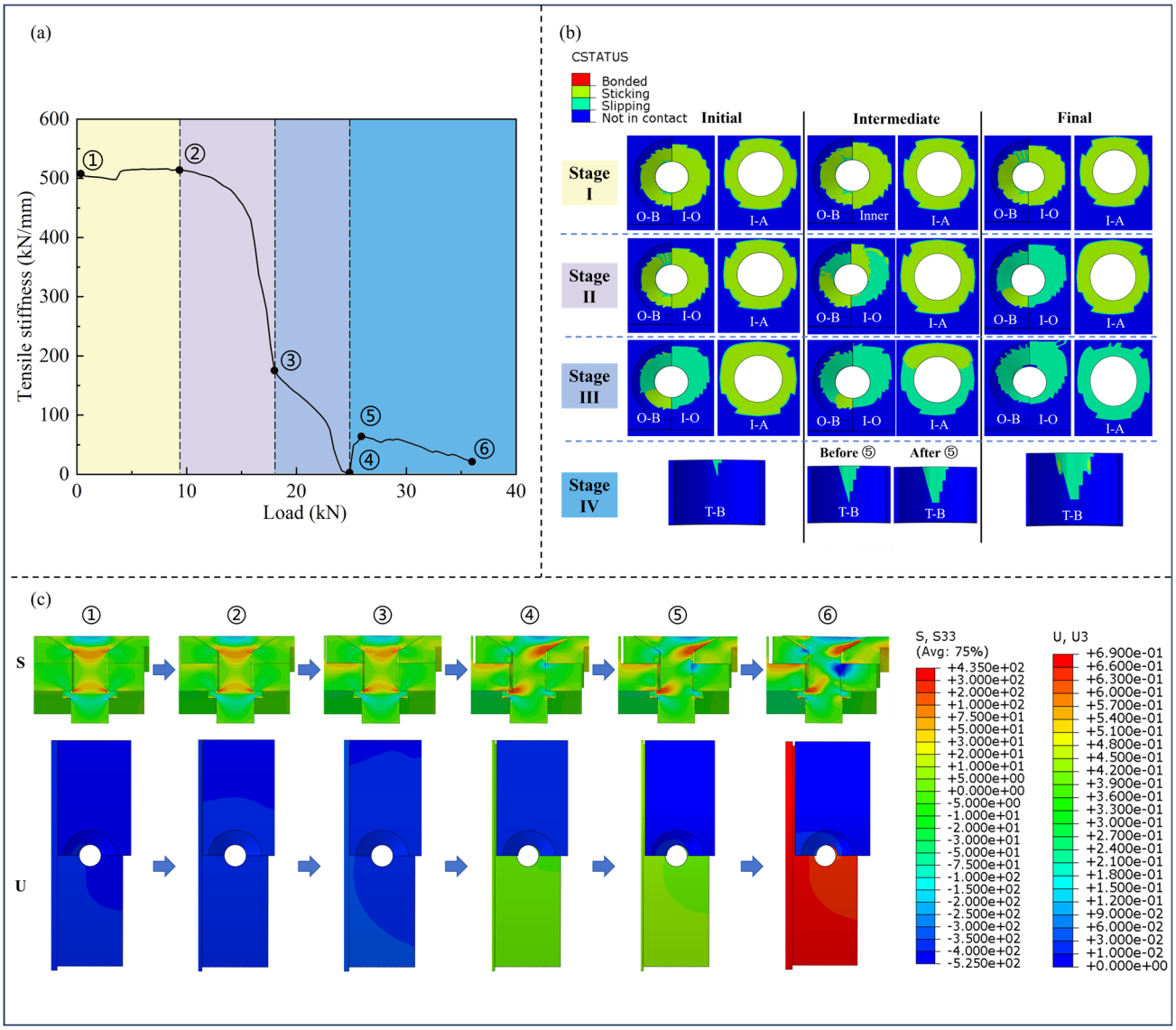


Figure 9. Evolution of structural (**a**) tensile stiffness, (**b**) contact state, and (**c**) axial stress (S33) (MPa)—axial deformation (U3) (mm) behavior of RBCCSJ under coupled axial tension and ambient temperature.

Stage III (Macroscopic sliding stage): With further loading up to approximately 24.84 kN, complete interfacial sliding develops between the ICS and OCS, marking the onset of macroscopic interface motion. This stage persists until direct contact occurs between the bolt shanks and the through-holes of the ICS, establishing a new load-transfer path and signifying a transition in the dominant mechanism from friction-controlled coupling to mechanically constrained transmission. The global tensile stiffness continues to decrease sharply (from about 1.75×10^2 kN/mm to 2.82 kN/mm) and the stiffness–load curve exhibits pronounced nonlinear curvature. This behavior indicates that as frictional resistance at the sliding interfaces diminishes, the rate of stiffness degradation accelerates

substantially. The degradation rate reaches its maximum during this stage, corresponding to the most unstable segment of the structural response.

Both the axial stress and deformation fields undergo substantial redistribution. The stress distribution along the bolts evolves from an initially symmetric pattern to an oblique orientation of approximately 30°, while prominent local stress concentrations appear near the ICS–OCS contact edges. The displacement contours reveal distinct sliding bands, confirming the occurrence of large-scale interfacial motion. The progressive loss of coordinated deformation between the ICS and OCS leads to partial mechanical decoupling, and the load-bearing mechanism consequently transitions to one dominated by direct contact constraint between the bolt shanks and the through-holes.

Stage IV (Mechanical load-bearing stage): Beyond ~24.84 kN, the fourth stage begins when the bolt shanks come into contact with the through-hole walls of the ICS. Upon initial contact (before special point 5), localized compressive interaction develops between the bolt shanks and the through-hole surfaces, forming a new mechanical constraint that effectively limits further axial elongation of the assembly. This contact engagement leads to a sharp rise in tensile stiffness (from 2.82 kN/mm to about 64.01 kN/mm) and the stiffness-load curve exhibits a pronounced positive curvature, reflecting enhanced load-bearing efficiency resulting from direct mechanical constraint and the progressive suppression of interfacial slip.

The axial displacement contours reveal localized deformation suppression near the through-hole regions, where steep displacement gradients contrast sharply with the surrounding areas, confirming the load redistribution effect induced by shank–hole compression. As the tensile load continues to increase, the contact compression zones expand radially along the through-hole circumference, promoting more uniform stress transfer between the bolts and the cylindrical shell. The axial stress field displays intensified compressive bands at the contact interfaces, accompanied by a noticeable reduction in tensile strain concentrations in adjacent shell regions. Once the compressed contact area stabilizes (after special point 5), the mechanical constraint reaches a steady state and the structural stiffness ceases to increase, indicating that the deformation response has transitioned from friction-dominated to geometrically constrained mechanical coupling. However, owing to the elastoplastic behavior of the material, the structural stiffness decreases linearly with increasing tensile load. By the end of the tensile phase, the stiffness ultimately reduces to 21.25 kN/mm. This stage marks the re-establishment of a stable load-transfer equilibrium following macroscopic interface motion.

Overall: The tensile stiffness exhibits a pronounced nonlinear evolution—an initial high plateau, a steep softening (Stages II–III), and a mechanical constraint recovery (Stage IV). These stages correspond to successive contact transitions (from full stick to partial slip to mechanical load-bearing). The overall stiffness variation spans a wide range, with the magnitude at different characteristic points differing by more than two order of magnitude (Specifically 536.12 kN/mm), as summarized in Table 5. This pronounced stiffness fluctuation underscores the high sensitivity of the structural response of the RBCCSJ to the evolving contact conditions and the dominant role of mechanical constraint transitions in governing its nonlinear tensile behavior.

Table 5. Characteristic tensile stiffness values of the RBCCSJ at representative load stages.

Special Points	Tensile Stiffness (kN/mm)	Corresponding Load (kN)
①	503	0.36
②	513	9.36
③	175	18

Table 5. *Cont.*

Special Points	Tensile Stiffness (kN/mm)	Corresponding Load (kN)
④	2.82	24.84
⑤	64.01	25.92
⑥	21.25	36

4.1.2. Under Different Heat Transfer Temperature Conditions

To further investigate the influence of transient heat transfer on the tensile stiffness behavior of RBCCSJ, and based on the analytical findings presented in Section 4.1.1, a series of coupled thermal–mechanical simulations is conducted to examine the evolution characteristics of structural stiffness under varying heat transfer durations. The analyzed conditions included transient heat transfer states at 2 s, 4 s, and 10 s, along with a steady-state thermal condition representing thermal equilibrium. The corresponding tensile stiffness–load evolution curves under these five thermal environments are illustrated in Figure 10.

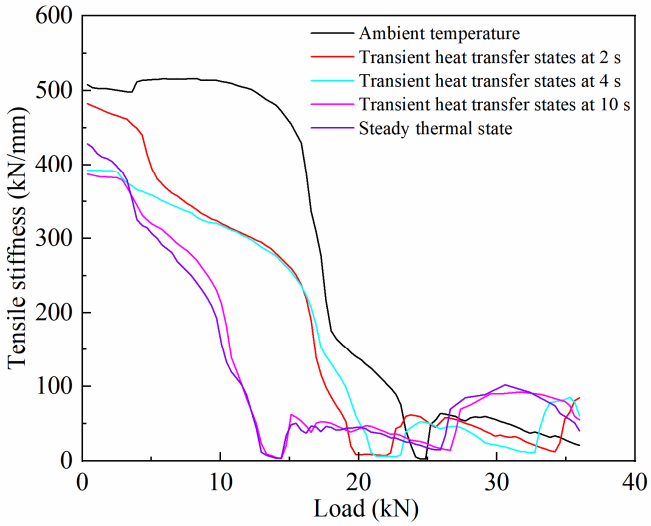


Figure 10. Tensile stiffness-load curves under different heat transfer conditions.

As shown in Figure 10, the tensile stiffness-load relationship of the RBCCSJ exhibits pronounced variations under different heat transfer durations, revealing a strong coupling between the thermal and mechanical fields that governs the stiffness evolution.

The four stages of nonlinear stiffness evolution observed under ambient conditions are also present under different heat transfer durations. However, elevated temperatures significantly reduce the overall stiffness, causing both the slip phase and the mechanical constraint phase to occur earlier. Following the mechanical load-bearing stage, a new **Stage V (Full Mechanical Coupling)** emerges, as illustrated in Figure 11.

Taking the steady-state thermal condition as an example, Stage V begins when the bolt shanks engage the countersinks of the OCS, establishing direct mechanical bearing contact at the shank–countersink interfaces and marking the onset of complete mechanical coupling within the assembly. Similarly to Stage IV, localized contact compression develops and progressively intensifies at the interface, with reduced axial displacement within the countersink region relative to adjacent areas. This mechanical constraint further suppresses axial elongation, resulting in a pronounced recovery of structural stiffness. The global tensile stiffness exhibits a second phase of rapid growth, increasing from approximately 14.87 kN/mm to about 102 kN/mm before declining due to material elastoplasticity. The stiffness–load curve displays an overall positive curvature during this transition, indicating

that the structure approaches full constraint under the combined action of the bolt-shank and countersink contacts.

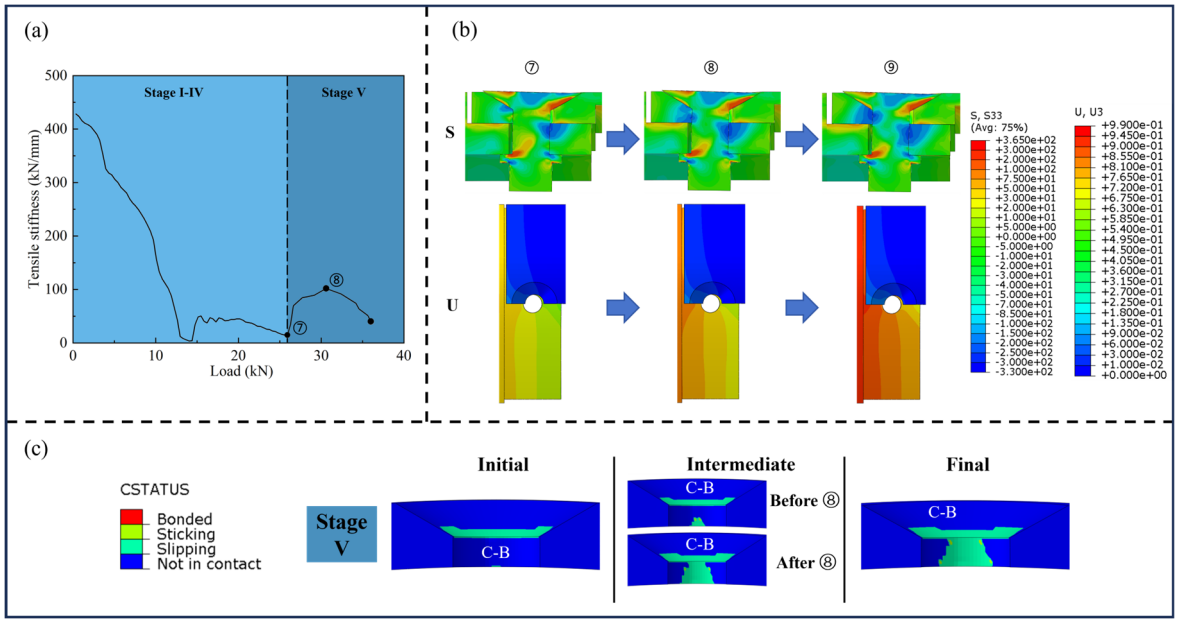


Figure 11. Evolution of structural (**a**) tensile stiffness, (**b**) contact state, and (**c**) axial stress (S33) (MPa)—axial deformation (U3) (mm) behavior of RBCCSJ under coupled axial tension and steady-state thermal conditions.

The axial stress field reveals concentrated compressive bands along the shank–countersink interfaces, accompanied by redistributed tensile stresses in the adjacent shell regions. These local compressive stresses counteract further tensile deformation, thereby restoring the coordinated load-bearing behavior of the ICS–OCS–bolt assembly. Displacement contours indicate that deformation becomes increasingly uniform as the contact compression area expands circumferentially and stabilizes.

Stage V thus signifies the establishment of complete mechanical load transfer, where the structural response transitions from partially constrained deformation to fully engaged constraint coupling. During subsequent tensile loading, no further interfacial evolution occurs, and the structural tensile stiffness decreases linearly solely due to the elastoplastic behavior of the material. Consequently, Stage V represents the final evolutionary state of the RBCCSJ under monotonic tension.

As shown in Figure 10, compared to the ambient case, the structural tensile stiffness under all heat transfer conditions shows the most significant reduction in the initial loading stage (up to ~126 kN/mm lower, ~24.6%). Moreover, temperature gradients induced by heat conduction notably influence the transition characteristics between stiffness stages, especially near the onset of Stage IV and Stage V, where the corresponding load differences reach approximately 10.44 kN relative to the ambient case and 8.28 kN relative to the steady-state thermal condition, respectively.

Under early transient heating (2 s and 4 s), evident temperature gradients develop between the bolts and the CCSs (Figure 8). The connecting members expand more rapidly than the bolts, inducing elevated interfacial compression and an axial stress up to +281.8 MPa within the bolt shanks (Figure 12). Compared with longer heat transfer durations, this additional compressive constraint enhances interfacial friction, delaying the onset of microslip and shifting the stiffness-load curve rightward. Consequently, during these initial transient heating stages, the structure temporarily maintains higher load-bearing capacity and delayed stiffness degradation.

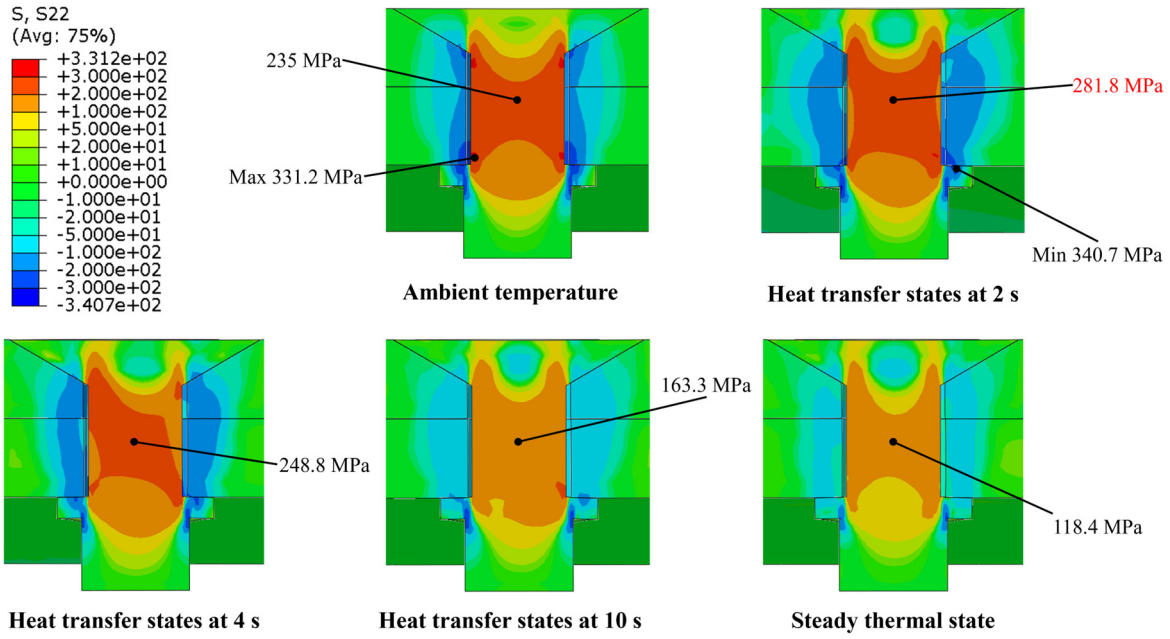


Figure 12. Radial stress (S22) cloud diagram of the cross-section of RBCCSJ under different heat transfer durations before loading (MPa).

After longer heating (10 s transient and steady-state thermal conditions), the temperature field becomes more uniform, and the mean temperature of both the bolts and CCSs increases substantially (Figure 8). The aluminum shell softens (elastic modulus, tensile strength, and yield strength decreases with temperature, Table 1), which dominates the stiffness reduction. The interface contact pressures drop, reducing frictional load transfer. As a result, the overall stiffness is lower under prolonged heating.

Physically, the structural stiffness is governed by two competing effects: thermal expansion mismatch (which boosts friction and stiffness in the short term) versus temperature-dependent softening (which lowers stiffness over time). The transition from a friction-dominated regime to a softening-dominated regime explains the temporal stiffness evolution. These thermo-mechanical coupling effects are critical in aerospace structures: neglecting transient heating can lead to underestimating stiffness loss and potential joint instability during service.

4.2. Mechanism of Effects on Compressive Stiffness

A compressive load (up to 36 kN) is applied similarly. The incremental compressive stiffness K^{C} is defined analogously to tension (Equation (3)).

$$\begin{cases} K_j^{C} = \frac{F_j^{C}-0}{u_j^{C}-0}, j = 1 \\ K_j^{C} = \frac{F_j^{C}-F_{j-1}^{C}}{u_j^{C}-u_{j-1}^{C}}, j = 2,3,\ldots,n \end{cases} \quad (3)$$

where F_j^{C} and u_j^{C} are the applied compressive load and the corresponding axial deformation at the j-th load increment, respectively; K_j^{C} is the corresponding compressive stiffness.

4.2.1. Under Ambient Temperature Conditions

The compressive stiffness-load curve, along with representative contact-state, stress, and deformation distributions, are shown in Figure 13. The overall compressive stiffness re-

sponse exhibits a distinct nonlinear evolution, which can be divided into four characteristic stages corresponding to different interfacial load transfer mechanisms.

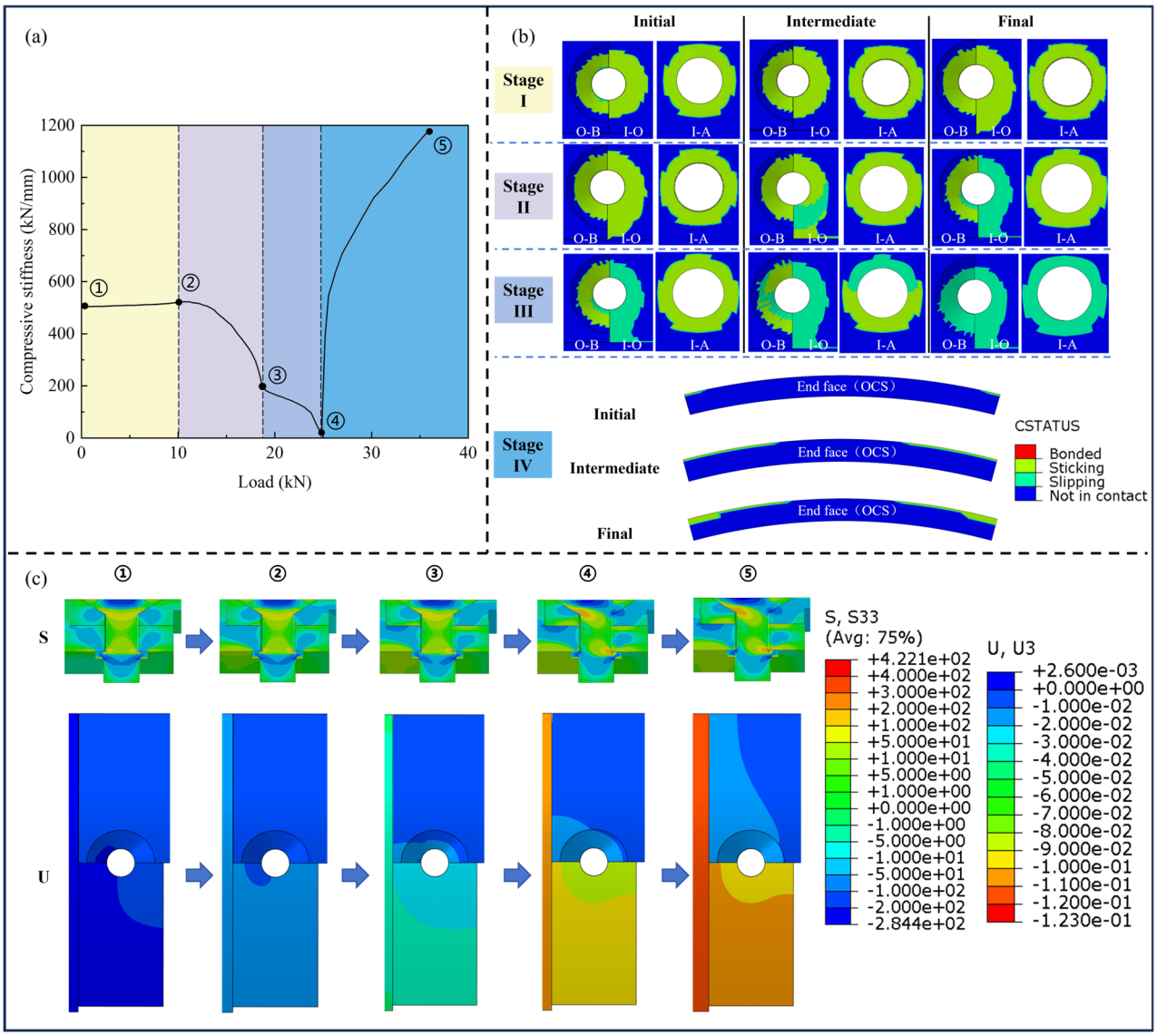


Figure 13. Evolution of structural (**a**) compressive stiffness, (**b**) contact state, and (**c**) axial stress (S33) (MPa)—axial deformation (U3) (mm) behavior of RBCCSJ under coupled axial compression and ambient temperature.

Stage I (Sticking stage): For small compression (from 0 kN to approximately 10.08 kN), the structural response remains nearly linear ($\approx 5.22 \times 10^2$ kN/mm). During this stage, the bolt preload dominates the contact constraint, maintaining full sticking at all main interfaces ('O–B', 'I–O', and 'I–A'). Only minor local compressive deformation occurs at the end face of ICS, and no significant interfacial slip is detected.

Stage II (Microslip initiation): This stage begins once the applied compressive load surpasses 10.08 kN. Localized relative slip first occurs at the 'I–O' interface, driven by nonuniform stiffness distribution and local stress concentration. As a result, the compressive stiffness decreases sharply from approximately 5.22×10^2 kN/mm to 1.98×10^2 kN/mm, marking the transition from a fully bonded to a partially slipping contact state. The corresponding contact-pressure field reveals evident redistribution, particularly near the outer edge of the 'I–O' interface, where the frictional constraint begins to deteriorate.

Stage III (Macroscopic sliding and contact reconfiguration): Upon exceeding a load of approximately 18.72 kN, extensive interfacial slipping develops, accompanied by local compression at the countersunk region of the bolt head. Unlike in the tensile case, the 'O–B' interface initially maintains sticking contact, preserving frictional constraint until the latter half of this stage, when shear-induced slip begins to occur. The overall compressive stiffness continues to decline, eventually stabilizing near 20.72 kN/mm. Concurrently, the axial stress field (Figure 11c) reveals that compressive stresses become concentrated in the upper portion of the bolt shank and the lower surface of the OCS, indicating a shift in the primary load-transfer path toward the shoulder region.

Stage IV (End-face engagement and stiffness recovery): This stage corresponds to the progressive compression and engagement of the ICS and OCS end faces. As the load increases beyond approximately 24.84 kN, the axial gap between the end faces gradually closes, forming a bearing-type contact region. The compressive load is then shared between the end-face interface and the bolt shank, while the contact area at the end-face expands progressively with increasing load. This results in a rapid rise in overall compressive stiffness, which reaches approximately 1.18×10^3 kN/mm The corresponding deformation contours clearly illustrate localized compression and engagement of the end regions, confirming the reconfiguration of the load-bearing mechanism.

In summary, the compressive stiffness evolution reflects a progressive transformation of the dominant load-transfer mechanism—from preload-controlled elastic coupling (Stage I) to friction-controlled partial slip (Stage II), macroscopic sliding and load-path redistribution (Stage III), and finally to bearing-type end-face compression (Stage IV). The overall compressive stiffness variation spans a wide range, with the magnitudes at different characteristic points differing by more than two orders of magnitude (specifically, from approximately 20.72 kN/mm to 1.18×10^3 kN/mm). Compared with the tensile process, stiffness recovery occurs more rapid and pronounced under compression owing to direct end-face engagement, which markedly enhances the load-carrying capacity, structural rigidity, and overall stability of the RBCCSJ.

4.2.2. Under Different Heat Transfer Temperature Conditions

Figure 14 presents the evolution of compressive stiffness with increasing load under various thermal conditions, including transient heat transfer durations of 2 s, 4 s, and 10 s, as well as the steady-state thermal condition.

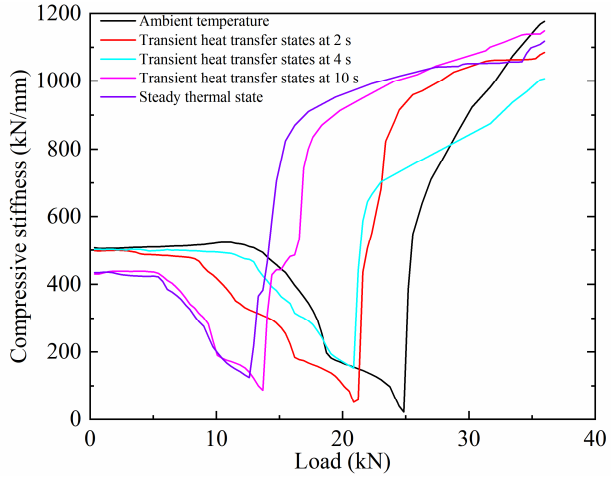


Figure 14. Compression stiffness–load curves under different heat transfer conditions.

As shown in Figure 14, the compressive stiffness–load relationships exhibit significant sensitivity to the thermal environment. The overall trend resembles that under ambient

conditions but shows distinct thermal coupling effects. The aluminum shell softens at elevated temperatures (Table 1), notably weakening the compressive stiffness during the sticking stage (prior to slip) across all heat transfer conditions. Quantitatively, the compressive stiffness in stage I under steady-state conditions decreases from approximately 522 kN/mm (at 25 °C) to about 422 kN/mm (at the steady thermal state), corresponding to a ~19.2% reduction. This reduction leads to an earlier onset of the slip phases (Stages II and III) and end-face contact, shifting the overall stiffness–load curve to the left.

In the early transient heating phase (2 s and 4 s), pronounced temperature gradients exist between the bolts and the surrounding connecting structures. The faster thermal expansion of the aluminum alloy structures relative to the steel bolts produces compressive interfacial thermal stresses, which in turn enhance local frictional resistance. This effect temporarily suppresses interfacial slip and delays the onset of macroscopic interface motion, thereby pronouncing the leftward shift in the stiffness-load curve (requiring approximately 8.28 kN higher load to reach special point 4 compared to steady-state conditions).

At the later loading stages (Stage IV), the competing effects of temperature-dependent modulus degradation and thermally induced interfacial pre-compression become evident. The former reduces the structure's intrinsic load-bearing capacity, while the latter increases the initial contact pressure at the end faces and shank interfaces. These two mechanisms counterbalance one another, causing the differences in compressive stiffness under various heat transfer conditions to progressively diminish with increasing compressive load.

In essence, the transient thermal–mechanical coupling induces a dual mechanism: (1) short-term frictional strengthening caused by thermal expansion mismatch and (2) long-term stiffness degradation driven by material softening. The balance between these effects determines the compressive stiffness evolution of the bolted connection under thermal loading. Such a mechanism has critical implications for aerospace structural design, indicating that transient aerodynamic heating can temporarily delay the reduction in structural stiffness before eventual material softening ultimately dominates the response.

4.3. Mechanism of Effects on Bending Stiffness

According to the ultimate overload and the structural dimensions of the cylindrical shells, a bending moment (up to 5 kN·m) is linearly and uniformly applied, and the rotation at the coupling point is measured. Bending stiffness K^{B} is defined by

$$\begin{cases} K_j^{\mathrm{B}} = \frac{M_j^{\mathrm{B}} - 0}{\theta_j^{B} - 0}, j = 1 \\ K_j^{\mathrm{B}} = \frac{M_j^{\mathrm{B}} - M_{j-1}^{\mathrm{B}}}{\theta_j^{\mathrm{B}} - \theta_{j-1}^{\mathrm{B}}}, j = 2, 3, \ldots, n \end{cases} \tag{4}$$

where M_j^{B} and θ_j^{B} are the applied moment load and the corresponding deflection angle at the j-th load increment, respectively, and all load increment is defined as 1% of the maximum applied bending moment; K_j^{B} is the corresponding bending stiffness.

4.3.1. Under Ambient Temperature Conditions

Figure 15 illustrates the axial displacement and stress distributions of the RBCCSJ under bending moment loading. The applied moment induces tension in half of the structure and compression in the other half, effectively dividing the assembly into tensile and compressive zones. Consequently, the overall bending stiffness is governed by the coupled response of the tensile stiffness in the upper region and the compressive stiffness in the lower region. The corresponding evolution of bending stiffness with increasing load is presented in Figures 16 and 17, which reveal that the structural response can be

divided into four distinct stages, each characterized by different interfacial contact and load-transfer mechanisms.

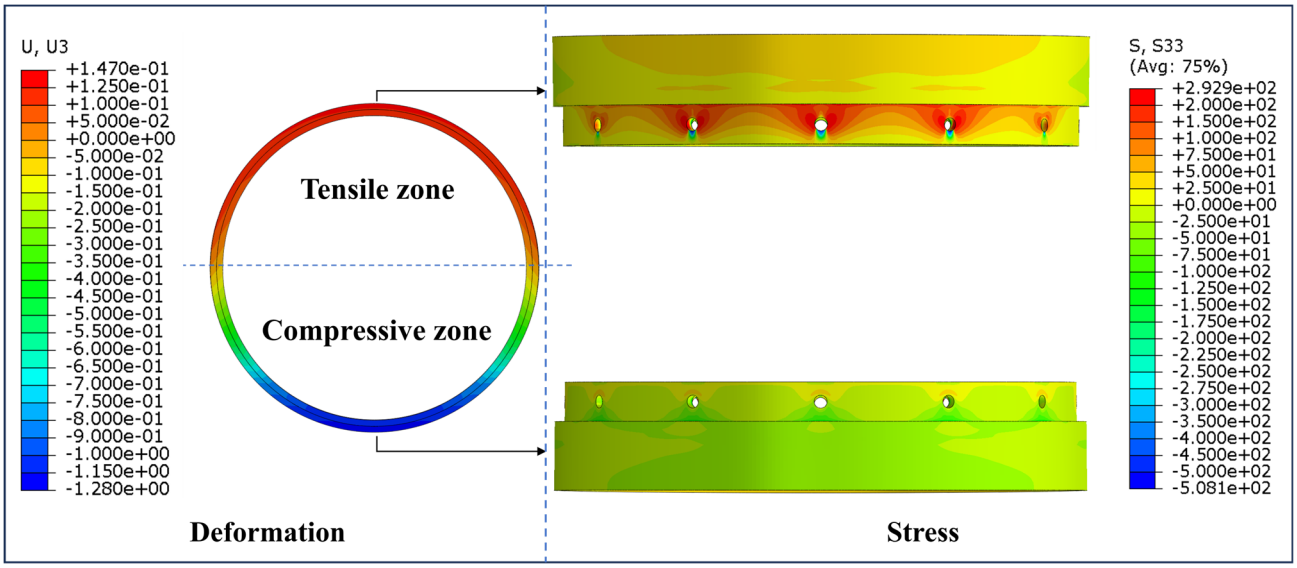


Figure 15. Axial displacement (U3) (mm) and axial stress (S33) fields (MPa) of the RBCCSJ under bending.

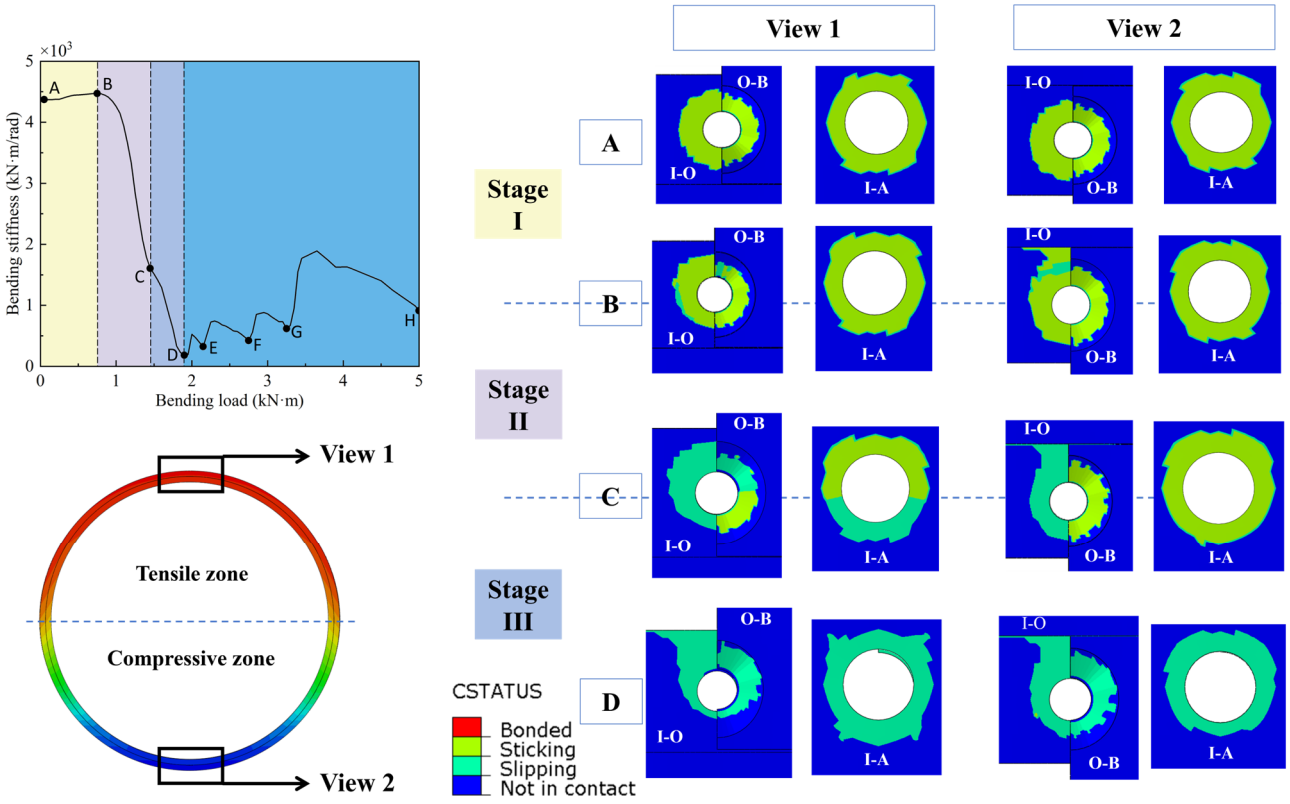


Figure 16. Evolution of structural bending stiffness and contact state of RBCCSJ under coupled bending moment and ambient temperature (Stage I–III).

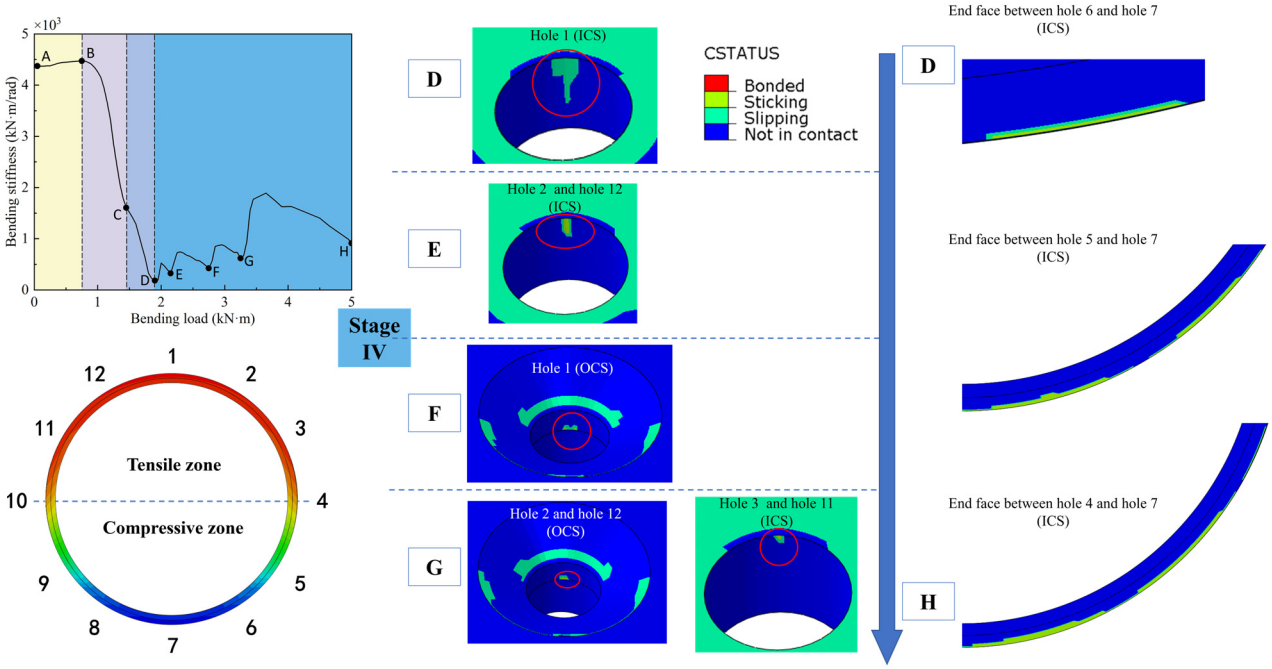


Figure 17. Evolution of structural bending stiffness and contact state of RBCCSJ under coupled bending moment and ambient temperature (Stage IV).

Stage I (Sticking stage): At the onset of bending, the structure undergoes localized elastic deformation as the applied moment gradually overcomes the initial bolt preload. Throughout this stage, The interfaces between the OCS and ICS (I–O), the OCS and bolt head (O–B), and the ICS and anchor nut (I–A) remain fully sticking, preserving complete interfacial coupling. Consequently, the bending stiffness remains high and nearly constant, with a value of approximately 4.47×10^3 kN·m/rad, representing the initial linear-elastic response regime of the structure.

Stage II (Microslip stage): As the bending moment increases to approximately 0.75 kN·m, the stiffness–bending moment curve exhibits a sharp downward transition, decreasing from about 4.47×10^3 kN·m/rad to 1.61×10^3 kN·m/rad. Localized microslip initiates at the I–O interface and gradually evolves into complete interfacial slip. Simultaneously, localized sliding develops at the O–B and I–A interfaces within the tensile region. The progressive loss of interfacial frictional restraint leads to the redistribution of the bolt preload and a reduction in load-transfer efficiency across the joint interfaces. In contrast, the O–B and I–A interfaces within the compressive region remain fully sticking, maintaining contact integrity and providing partial restraint that mitigates excessive bending deformation. Consequently, this stage is characterized by asymmetric deformation between the tensile and compressive zones, resulting in a pronounced reduction in overall bending stiffness.

Stage III (Macroslip stage): As the bending moment increases to approximately 1.45 kN·m, extensive macroslip develops across all major contact interfaces. Within the compressive zone, localized contact loss initiates near the outer-edge regions, further weakening the interfacial constraint. The frictional load-transfer capacity deteriorates rapidly, leading to a substantial reduction in overall bending stiffness, which reaches a minimum value of approximately 0.18×10^3 kN·m/rad. At this stage, the dominant deformation mechanism transitions from interfacial friction control to bolt–through-hole engagement, signifying a shift from distributed frictional coupling to discrete bearing and shank compression as the primary load-transfer mode.

Stage IV (Through-hole engagement and face contact stage): At higher bending moments exceeding approximately 1.9 kN·m, additional contact mechanisms are progressively activated. The bolts in the tensile zone begin to engage with the through-hole walls of the ICS, while in the compressive zone, the ICS and OCS establish direct face contact. These new contact states significantly restrict further deformation, resulting in a rapid increase in overall structural stiffness. At special point G, the simultaneous formation of two new contact pairs results in the greatest enhancement of the structural bending stiffness within this stage, reaching approximately 1.89×10^3 kN·m/rad. The sequential engagement of bolts with the through-hole walls produces discrete stiffness jumps, whereas the progressive expansion of face contact within the compressive zone leads to gradual stabilization of the stiffness response. Once all bolt–hole and face contacts reach equilibrium, the bending stiffness no longer increases. Instead, it declines steadily as the zones of material yielding progressively expand within the structure, marking the establishment of full mechanical coupling under bending loads.

In summary, the bending stiffness evolution of the RBCCSJ exhibits a distinct multi-stage nonlinear behavior, governed by sequential transitions in interfacial contact conditions. The structural stiffness initially remains high during the sticking stage, then decreases sharply through microslip and macroslip before recovering as bolt-through-hole and face contact become dominant, and finally enters a phase of sustained decline as the material enters the elasto-plastic stage. The overall stiffness variation spans nearly one order of magnitude (from ~0.18×10^3 to 4.47×10^3 kN·m/rad). This nonlinear evolution underscores the critical role of interfacial contact reconfiguration in governing the bending response of bolted cylindrical shell joints and provides valuable insight for predicting stiffness reliability in aerospace structural design under complex bending loads.

4.3.2. Under Different Heat Transfer Temperature Conditions

Figure 18 compares the bending stiffness–moment relationships of the RBCCSJ under various transient and steady-state thermal conditions. The overall bending evolution during Stages I–III closely mirrors the tensile and compressive behaviors discussed earlier. Specifically, the thermal softening of the material at elevated temperatures (as listed in Table 1) leads to a monotonic decrease in overall bending stiffness with increasing heat transfer duration. Quantitatively, the maximum bending stiffness under ambient temperature exceeds that under the steady thermal state by approximately 34%. This promotes earlier slip and shifts the stiffness–load curve to the left. Meanwhile, thermally induced stresses enhance interfacial friction between the I–O members, temporarily suppressing interfacial slip and delaying the onset of stage transitions. This phenomenon mitigates the leftward shift in the stiffness–moment curve, most evident at the 2 s and 4 s transient states. As heat transfer progresses and the temperature field becomes more uniform (at 10 s transient and steady-state conditions), the enhanced friction effect diminishes, and the stiffness–moment response converges toward that of the steady-state condition.

From a physical standpoint, this thermo-mechanical coupling behavior reflects the competition between two opposing mechanisms: (1) thermal-stress-induced frictional stiffening, which dominates during the early transient heating stages, and (2) temperature-dependent material softening, which becomes dominant during prolonged thermal exposure. The transition between these mechanisms delineates the temporal evolution of bending stiffness degradation in thermally loaded bolted cylindrical structures. These findings provide important insights into the deformation control, thermal resilience, and stiffness reliability of radially bolted assemblies operating under transient aerodynamic heating environments.

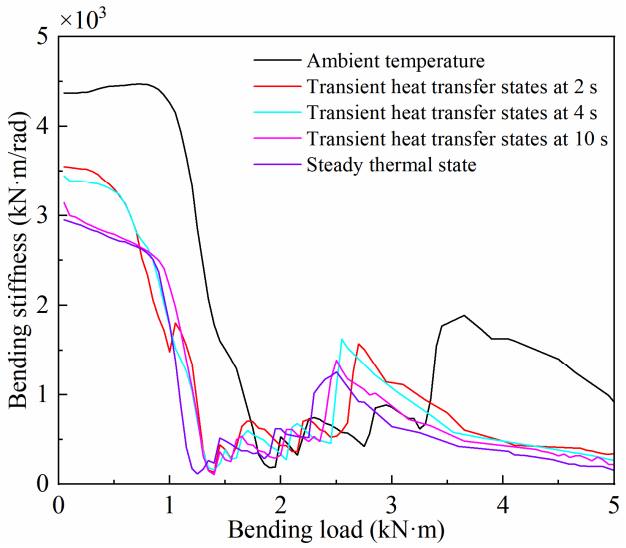


Figure 18. Bending stiffness–load curves under different heat transfer conditions.

5. Conclusions

This study employed a high-fidelity, sequentially coupled thermo–mechanical finite-element framework to investigate the stiffness-evolution mechanisms of a representative radially bolted cylindrical–cylindrical shell structure under combined transient heating and mechanical loads (tension, compression, and bending). The principal conclusions are summarized as follows:

(1) Sequential contact transitions (from full sticking → microslip → macroslip → mechanical bearing) govern the nonlinear stiffness evolution under tensile, compressive, and bending loads. These transitions produce pronounced segmented nonlinear responses, manifested as distinct "stiffness valleys". Under tension and bending, the maximum stiffness occurs in the fully sticking stage, whereas under compression it appears when the structural components achieve complete end-face bearing. The minimum stiffness in all cases corresponds to full interfacial slip, and the overall stiffness variation exceeds two orders of magnitude (maximum differences: ≈510.18 kN/mm for tension, ≈501.28 kN/mm for compression, ≈4.29 × 10^3 kN·m/rad for bending). This reflects the dominance of interfacial slip and bearing re-engagement in controlling load transfer.

(2) The mechanisms of stiffness reduction and recovery differ across loading modes. Stiffness degradation arises primarily from the loss of frictional restraint as external loads overcome the bolt-preload-induced interface friction. Recovery mechanisms, however, are distinct: under tension, stiffness is restored through bolt-shank and countersink engagement; under compression through end-face-bearing formation; and under bending through the combined activation of bolt–hole contact in the tensile zone and face compression in the compressive zone.

(3) Transient aerodynamic heating modifies stiffness evolution through two competing thermo–mechanical effects: (a) thermal expansion mismatch, which transiently increases interfacial compressive pressure and friction, resulting in short-term stiffening and delayed slip onset; and (b) temperature-dependent material softening, which decreases structural stiffness during prolonged heating. Quantitatively, this study reveals reductions of up to 24.6% in early-stage tensile stiffness, 19.2% in sticking stage compressive stiffness, and 34% in maximum bending stiffness under steady thermal conditions compared with ambient temperature. These results highlight the sensitive interplay between frictional stiffening and material softening during transient thermal exposure.

(4) Overall, the RBCCSJ exhibit highly nonlinear and temperature-sensitive stiffness behavior governed by evolving contact conditions. For aerospace vehicle structures subjected to transient heating and variable mechanical loads, neglecting these thermo–mechanical contact effects can lead to significant errors in stiffness prediction, dynamical characterization, and structural reliability assessment. Integrating contact evolution and transient thermal effects into structural design, modeling, and certification workflows will substantially enhance the fidelity of stiffness evaluation and improve the safety margins of aerospace structures.

Author Contributions: Conceptualization, N.G.; Methodology, N.G. and W.Y.; Validation, W.Y.; Investigation, W.Y. and S.Z.; Writing—original draft, N.G., W.Y., S.Z. and H.D.; Writing—review & editing, N.G.; Visualization, H.D.; Project administration, C.X.; Funding acquisition, C.X. All authors have read and agreed to the published version of the manuscript.

Funding: This research was funded by [National Natural Science Foundation of China] grant number [No. 12072268].

Data Availability Statement: Data is contained within the article.

Conflicts of Interest: The authors declare no conflict of interest.

References

1. Yay, Ö.; Kunt, G.; Gürgen, S. Bolted joints in aerospace structures. In *Joining Operations for Aerospace Materials*; Gürgen, S., Ed.; Sustainable Aviation; Springer Nature: Cham, Switzerland, 2024; pp. 41–53.
2. Zhang, S.; Guo, N.; Xu, C. Experimental and numerical investigations into tensile and compressive behavior of radial countersunk screw lap joints. *Int. J. Non-Linear Mech.* **2025**, *177*, 105159. [CrossRef]
3. Gharouni, S.M.; Panahiha, H.M.; Jam, J.E. Space Shuttle solid rocket motor (SRM) field joint: Review paper. *Metall. Mater. Eng.* **2014**, *20*, 155–163. [CrossRef]
4. Chakhari, J.; Daidié, A.; Chaib, Z.; Guillot, J. Numerical model for two-bolted joints subjected to compressive loading. *Finite Elem. Anal. Des.* **2008**, *44*, 162–173. [CrossRef]
5. Chaves, C.E.; Fernandez, F.F. A review on aircraft joints design. *Aircr. Eng. Aerosp. Technol.* **2016**, *88*, 411–419. [CrossRef]
6. Umakanth, M.; Kumar, P.U.; Narayanamurthy, V.; Korla, S. Predicting the rotational compliance of a flight inter-section joint. *NMIMS J. Eng. Technol. Rev.* **2021**, *3*, 62–73.
7. Umakanth, M.; Kumar, P.U.; Narayanamurthy, V.; Korla, S. Influence of number of studs on compliance of a flight intersection joint. *IOP Conf. Ser. Mater. Sci. Eng.* **2021**, *1166*, 012050. [CrossRef]
8. Umakanth, M.; Kumar, P.U.; Narayanamurthy, V.; Korla, S. Axial stiffness of a slot-nut type conformal segment joint. In *Recent Advances in Applied Mechanics*; Tadepalli, T., Narayanamurthy, V., Eds.; Lecture Notes in Mechanical Engineering; Springer: Singapore, 2022; pp. 367–377.
9. Umakanth, M.; Kumar, P.U.; Narayanamurthy, V.; Korla, S. Modelling the joint rotational compliance of stud-pocket type flight inter-section joint. *Thin-Walled Struct.* **2023**, *185*, 110565. [CrossRef]
10. Tang, Q.; Li, C.; She, H.; Wen, B. Vibration analysis of bolted joined cylindrical-cylindrical shell structure under general connection condition. *Appl. Acoust.* **2018**, *140*, 236–247. [CrossRef]
11. Vadean, A.; Leray, D.; Guillot, J. Bolted joints for very large bearings—Numerical model development. *Finite Elem. Anal. Des.* **2006**, *42*, 298–313. [CrossRef]
12. Li, X.; Zhang, X.; Wang, R.; Wang, W. Study on the behavior of sunk screw connection between cabins in the rocket. *Acta Astronaut.* **2020**, *166*, 199–208. [CrossRef]
13. Zhang, X.; Wang, R.; Li, X.; Lu, C.; Wang, Z.; Wang, W. Dynamics modeling and characterization of sunk screw connection structure in small rockets. *Aerospace* **2022**, *9*, 648. [CrossRef]
14. Mohapatra, R.; Palathingal, S.; Narayanamurthy, V.; Ramji, M. Modeling of counter-bore and counter-sink screw lap joints. *Mech. Based Des. Struct. Mach.* **2024**, *52*, 289–314. [CrossRef]
15. Li, D.; Xu, C.; Li, R.; Zhang, W. Contact parameters evolution of bolted joint interface under transversal random vibrations. *Wear* **2022**, *500–501*, 204351. [CrossRef]
16. Li, D.; Botto, D.; Li, R.; Xu, C.; Zhang, W. Experimental and theoretical studies on friction contact of bolted joint interfaces. *Int. J. Mech. Sci.* **2022**, *236*, 107773. [CrossRef]

17. Yang, H.; Xu, C.; Guo, N. Modelling tangential friction considering contact pressure distribution of rough surfaces. *Mech. Syst. Signal Process.* **2023**, *198*, 110406. [CrossRef]
18. Verwaerde, R.; Guidault, P.-A.; Boucard, P.-A. A non-linear finite element connector model with friction and plasticity for the simulation of bolted assemblies. *Finite Elem. Anal. Des.* **2021**, *195*, 103586. [CrossRef]
19. Sehgal, A.K.; Juneja, C.; Singh, J.; Kalsi, S. Comparative analysis and review of materials properties used in aerospace industries: An overview. *Mater. Today Proc.* **2022**, *48*, 1609–1613. [CrossRef]
20. Trofimov, E.A.; Lutfullin, R.Y.; Kashaev, R.M. Elastic properties of the titanium alloy Ti-6Al-4V. *Lett. Mater.* **2015**, *5*, 67–69. [CrossRef]
21. Ibrahim, R.A.; Pettit, C.L. Uncertainties and dynamic problems of bolted joints and other fasteners. *J. Sound Vib.* **2005**, *279*, 857–936. [CrossRef]
22. Hu, J.; Zhang, K.; Cheng, H.; Qi, Z. Mechanism of bolt pretightening and preload relaxation in composite interference-fit joints under thermal effects. *J. Compos. Mater.* **2020**, *54*, 4929–4946. [CrossRef]
23. Mayeaux, B.M.; Collins, T.E.; Jerman, G.A.; McDanels, S.J.; Piascik, R.S.; Russell, R.W.; Shah, S.R. Materials analysis: A key to unlocking the mystery of the Columbia tragedy. *JOM* **2004**, *56*, 20–30. [CrossRef]
24. Alkatan, F.; Stephan, P.; Daidie, A.; Guillot, J. Equivalent axial stiffness ofvarious components in bolted joints subjected to axial loading. *Finite Elem. Anal. Des.* **2007**, *443*, 589–598. [CrossRef]
25. Li, X.; Zhang, X. The strength analysis of steel sunk screw connections in the rocket. *Acta Astronaut.* **2017**, *137*, 345–352. [CrossRef]
26. Mohapatra, R.; Palathingal, S.; Narayanamurthy, V.; Ramji, M. Modeling the mechanical behavior of torque-tightened screw lap joints. *Eng. Struct.* **2024**, *298*, 117071. [CrossRef]
27. Mohapatra, R.; Palathingal, S.; Narayanamurthy, V.; Ramji, M. Modeling the joint rotational stiffness of a radial-type flight intersection joint: An analytical approach, numerical simulation, and experimental validation. *Thin-Walled Struct.* **2024**, *196*, 111473. [CrossRef]
28. Mohapatra, R.; Palathingal, S.; Narayanamurthy, V.; Ramji, M. Investigating the influence of pre-tightening on radial-type flight intersection joints using a spring-mass model. *Proc. Inst. Mech. Eng. Part. G J. Aerosp. Eng.* **2025**, *239*, 702–723. [CrossRef]
29. Marek, P.; Pawlicki, J.; Mościcki, A. Tightness problems at the flange connection in transient temperature and high pressure condition. *Eng. Fail. Anal.* **2022**, *133*, 105986. [CrossRef]
30. Abid, M. Determination of safe operating conditions for gasketed flange joint under combined internal pressure and temperature: A finite element approach. *Int. J. Press Vessels Pip.* **2006**, *83*, 433–441. [CrossRef]
31. Omiya, Y.; Sawa, T. Thermal stress analysis and the sealing performance evaluation of bolted flange connection at elevated temperature. In Proceedings of the ASME 2009 Pressure Vessels and Piping Conference, Prague, Czech Republic, 26–30 July 2009; High Pressure Technology; Nondestructive Evaluation Division; Student Paper Competition; ASMEDC: New York, NY, USA, 2009; Volume 5, pp. 397–408.
32. Sawa, T.; Muramatsu, A.; Kumano, H. Mechanical behavior of bolted joints under thermal changes. In *Reliability, Stress Analysis, and Failure Prevention Aspects of Adhesive and Bolted Joints, Rubber Components, Composite Springs*; American Society of Mechanical Engineers: New York, NY, USA, 1998; pp. 141–150.
33. Jaglinski, T.; Lakes, R. Creep behavior of Al-Si Die-Cast alloys. *J. Eng. Mater. Technol.* **2004**, *126*, 378–383. [CrossRef]
34. Jaglinski, T.; Nimityongskul, A.; Schmitz, R.; Lakes, R.S. Study of bolt load loss in bolted aluminum joints. *J. Eng. Mater. Technol.* **2007**, *129*, 48–54. [CrossRef]
35. Kettler, K.; Klenk, A.; Weihe, S. Experimental and numerical investigations on the relaxation behavior of power plant flange connections under steady state and transient conditions. *J. Press Vessel Technol.* **2024**, *146*, 041302. [CrossRef]
36. Coman, C.D.; Constantinescu, D.M. Temperature effects on joint strength and failure modes of hybrid aluminum–composite countersunk bolted joints. *Proc. Inst. Mech. Eng. Part J. Mater. Des. Appl.* **2019**, *233*, 2204–2218. [CrossRef]
37. Coman, C.D. Thermal influence on the stiffness of hybrid metal-composite countersunk bolted joints. *INCAS Bull.* **2021**, *13*, 35–45. [CrossRef]
38. Sasikumar, A.; Guerrero, J.; Quintanas-Corominas, A.; Costa, J. Numerical study to understand thermo-mechanical effects on a composite-aluminum hybrid bolted joint. *Compos. Struct.* **2021**, *275*, 114396. [CrossRef]
39. Madhusudana, C.V. *Thermal Contact Conductance*; Springer: New York, NY, USA, 1996.
40. Childs, P.R.N. Fastening and power screws. In *Mechancial Design Engineering Handbook*; Elsevier: Amsterdam, The Netherlands, 2014; pp. 677–719.

Disclaimer/Publisher's Note: The statements, opinions and data contained in all publications are solely those of the individual author(s) and contributor(s) and not of MDPI and/or the editor(s). MDPI and/or the editor(s) disclaim responsibility for any injury to people or property resulting from any ideas, methods, instructions or products referred to in the content.